**Atmospheric
Chemistry
and Physics**

Increase of upper troposphere/lower stratosphere wave baroclinicity during the second half of the 20th century

J. M. Castanheira[1], **J. A. Añel**[1,2], **C. A. F. Marques**[1], **J. C. Antuña**[3], **M. L. R. Liberato**[4,5], **L. de la Torre**[1,2], and **L. Gimeno**[2]

[1]CESAM, Department of Physics, University of Aveiro, Aveiro, Portugal
[2]EPhysLab, Faculty of Sciences of Ourense, University of Vigo, Ourense, Spain
[3]Estación Lidar de Camagüey, Camagüey, Cuba
[4]Department of Physics, University of Trás-os-Montes e Alto Douro, Vila Real, Portugal
[5]CGUL, IDL, University of Lisbon, Lisbon, Portugal

Abstract. A strengthening of the equatorward temperature gradient in the upper troposphere/lower stratosphere (UTLS), at subtropics and midlatitudes, is consistently reproduced in several modelling studies of the atmospheric response to the increase of greenhouse gas radiative forcing. Some of those studies suggest an increase of the baroclinicity in the UTLS region because of the enhanced meridional temperature gradient.

This study presents observational evidence of an increase of the baroclinic wave components of UTLS circulation (UTLS wave baroclinicity), during the second half of the 20th century. The evidence is given by significant positive trends in the energy of baroclinic normal modes of the NCEP/NCAR reanalysis, and significant positive trends in the UTLS eddy available potential energy of the NCEP/NCAR, ERA-40, NCEP-2 and JRA-25 reanalyses. Significant positive trends in the frequency of double tropopause events in radiosonde data are also interpreted as a manifestation of an increase of the UTLS wave baroclinicity.

1 Introduction

In an assessment of several coupled chemistry-climate models, Eyring et al. (2006) showed that all models consistently simulate a stratospheric cooling trend during the second half of the 20th century. Using the GFDL coupled atmosphere-ocean-land climate model, Schwarzkopf and Ramaswamy (2008) showed a similar cooling trend of the stratosphere and a warming trend of the troposphere. Additionally, the general features of the simulated temperature trends are in agreement with observed trends (Randel et al., 2009).

Moreover, it is well known that the changeover from tropospheric warming to stratospheric cooling occurs at lower altitudes in the extratropics due to the fact that the tropical tropopause is higher than the extratropical one. Thus, the deep warming of the tropical troposphere and the cooling of the lower extratropical stratosphere leads to the strengthening of the meridional thermal gradients in the upper troposhere/lower stratosphere (UTLS) at the subtropical and midlatitudes (e.g. Garcia and Randel, 2008; Ramaswamy and Schwarzkopf, 2002, for simulations) and (Kanukhina et al., 2008; Allen and Sherwood, 2008; Randel et al., 2009, for observations). This strengthening of the meridional thermal gradients will cause an increase of baroclinicity in the subtropical and midlatitude UTLS regions (Eichelberger and Hartmann, 2005). In fact, model simulations of the temperature response to increasing radiative greenhouse gas forcing show a decrease of lower troposphere large-scale baroclinicity at middle latitudes and an increase of baroclinicity of the UTLS at the same latitudes (Geng and Sugi, 2003, and references therein). The decrease of lower troposphere baroclinicity, in the Northern Hemisphere (NH), is mainly attributed to the decrease of near surface meridional temperature gradient, which is explained by the fact that, when global warming happens, the high latitudes usually warm more than the lower latitudes due to the positive feedback of sea ice and snow cover in winter (Geng and Sugi, 2003).

Based on the above mentioned studies, our hypothesis is that global warming must be associated with a change of the vertical structure of baroclinicity, i.e with an increase of upper levels baroclinic instability and a reduction of lower levels baroclinic instability. Anomalies generated near the tropopause and near the surface present different vertical structures (e.g. Hoskins et al., 1985, see their Figs. 15 and 16); and it may also be expected that baroclinic waves excited in the UTLS have larger horizontal and vertical scales than the ones of baroclinic waves associated with near surface temperature gradients (Thorpe, 1985; Juckes, 1999). Then the change of baroclinicity must manifest itself in a change of the vertical structures of the most excited/amplified baroclinic waves. Accordingly, a study of the trends in the energy associated with baroclinic waves decomposed on a basis of vertical structure functions seems adequate to test our hypothesis. Results will show that an increase (decrease) of the UTLS large (lower troposphere small) vertical-scale wave baroclinicity, may be already diagnosed during the second half of the 20th century both in reanalyzed data and in radiosonde data.

2 Data and method

2.1 Normal mode expansion

Part of the study is based on NCEP/NCAR reanalysis and covers the 1958–2006 period. We analyzed the NH cool season (November to April) daily means of the horizontal wind components (u, v) and of the geopotential height, available on 17 standard pressure levels from 1000 to 10 hPa, on a $2.5° \times 2.5°$ horizontal grid.

The global horizontal wind (u, v) and geopotential(ϕ) fields were expanded in terms of the normal modes of the NCEP/NCAR reference atmosphere (see Liberato et al., 2007, and references therein for details), i.e.,

$$\begin{bmatrix} u \\ v \\ \phi \end{bmatrix} = \sum_{m=0}^{\infty} \sum_{s=-\infty}^{\infty} \sum_{l=0}^{\infty} \sum_{\alpha=1}^{3} w_{msl}^{\alpha}(t) \, G_{m(p)} \, \exp(is\lambda) \mathbf{C}_m \qquad (1)$$
$$\cdot \begin{bmatrix} U(\theta) \\ i V(\theta) \\ Z(\theta) \end{bmatrix}_{msl,\alpha}$$

where λ, θ and p are the longitude, latitude and pressure, respectively. The functions $G_m(p)$ represent separable vertical structures, and $\mathbf{C}_m = \mathrm{diag}[(gh_m)^{1/2}, (gh_m)^{1/2}, gh_m]$ is a diagonal matrix of scaling factors, with g representing the earth's gravity and h_m the equivalent heights. Each horizontal structure function is given by the product of a zonal wave with wavenumber s and a vector $[U(\theta), i V(\theta), Z(\theta)]^T_{msl,\alpha}$ which defines the meridional profile of the wave, where l is a meridional index which may be regarded as an indicator of the meridional scale of the motion. The index $\alpha=1, 2, 3$ refers to westward traveling inertio-gravity waves, Rossby waves and

eastward traveling inertio-gravity waves, respectively. The coefficients $w_{msl}^{\alpha}(t)$ are the complex amplitudes, where t is the time.

Each vertical structure $G_m(p)$ has m nodes, with $m=0$ and $m \geq 1$ denoting barotropic and baroclinic vertical structures, respectively (Fig. 1). The equivalent heights h_m decrease with the index m, and we will refer to the modes with $m<5$ as the deeper modes and modes with $m>5$ as the shallower modes. As it may be observed in Fig. 1, the vertical structures of the first four baroclinic modes ($m<5$) have the largest amplitudes and their nodes in the UTLS and above, whereas the shallower baroclinic modes ($m>5$) have larger amplitude and several nodes in the lower troposphere. These features make the deeper baroclinic modes more sensitive to the UTLS and middle stratosphere circulation variability, whereas the shallower baroclinic modes will be relatively more sensitive to lower troposphere circulation variability. It may also be observed in Fig. 1 that the shallower baroclinic modes ($m>5$) have smaller vertical scales (their nodes are closer) both in the troposphere and in the stratosphere. In fact, the vertical index m can be regarded as a kind of vertical wave number. Then, it is expected that small vertical scale anomalies, both in the troposphere and in the stratosphere, will project on the shallower baroclinic modes, i.e, on the modes of higher vertical wave numbers. This means that the projection on the vertical structures allows for a filtering based on the vertical scale of the anomalies (see Appendix A for more details.)

The total (i.e. kinetic + available potential) energy of each normal mode is proportional to the square of its amplitude $\left(E_{msl}^{\alpha}(t) \propto |w_{msl}^{\alpha}(t)|^2\right)$; and the energy $E_m(t)$, associated with a given vertical structure m and a given subset of wave numbers ($1 \leq s \leq N$) of Rossby or gravity type, is obtained by summing the energy associated with all meridional indices l for the N wave numbers.

The energy of the NCEP/NCAR reanalysis was calculated for both daily coefficients $w_{msl}^{\alpha}(t)$ and low pass filtered (period>10 days) coefficients. Afterwards, energy of high frequency waves was derived as the differences between the energies calculated with unfiltered and with low pass filtered $w_{msl}^{\alpha}(t)$ coefficients. Finally, for each energy time series $E_m(t)$, a linear trend was calculated applying a least square deviation fit to the November–April means in the 1958–2006 period.

A strengthening of the equatorward gradient of the UTLS zonal mean temperature was already diagnosed in the NCEP/NCAR reanalysis (Kanukhina et al., 2008). Then, one could try to assess the trend in the baroclinicity using the Eady growth-rate maximum, $\sigma_{BI} \cong 0.31 \, (g/T \, N) \, |\nabla T|$, where T is the temperature, and N is the Brunt-Väisälä frequency (Geng and Sugi, 2003, and references therein). However, UTLS temperatures in reanalysis data are sensitive to changes in assimilation input data, in particular the inclusion of satellite data beginning in 1979, and they are not suitable for the study of the UTLS baroclinicity trend (Allen and
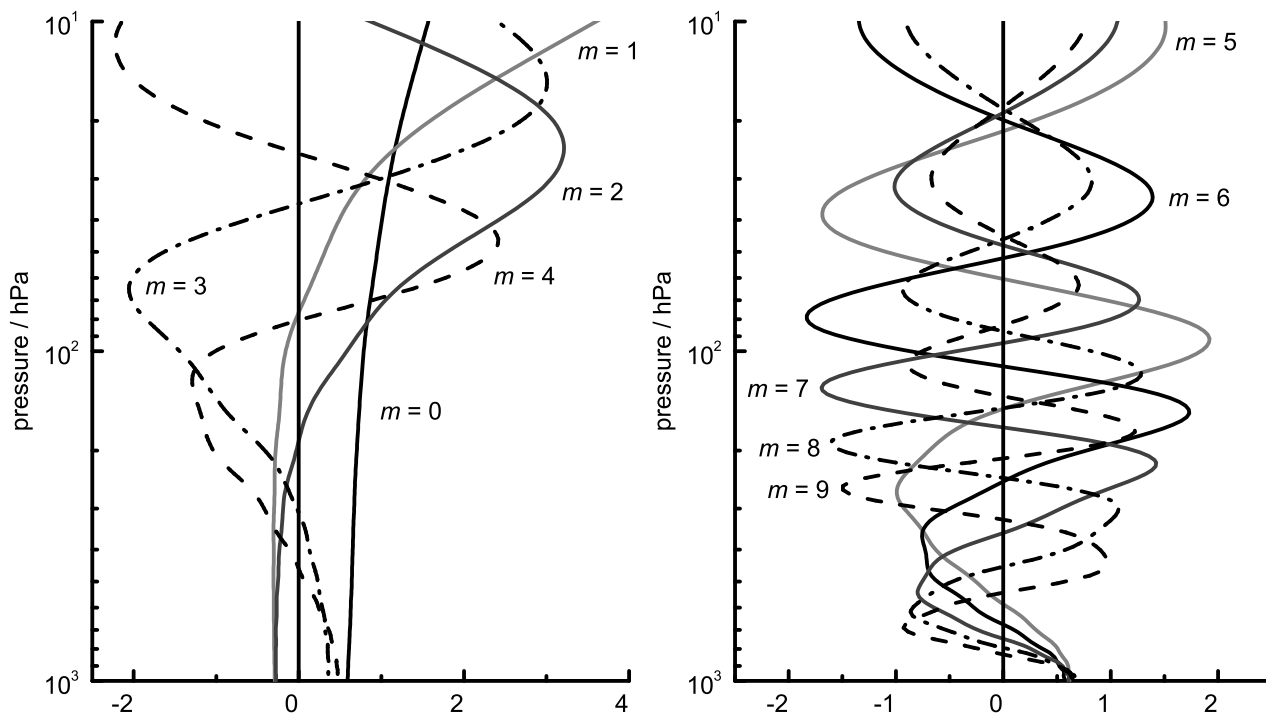
Fig. 1. Vertical structure functions of the barotropic (m=0) and first nine baroclinic modes (m=1,...,9) of the NCEP/NCAR atmosphere. For $m \geq 2$ one node appears above 10 hPa and it is not represented.

Sherwood, 2008; Randel et al., 2009). Although we expect that normal mode energy will be more resilient to the data inhomogeneities because it accounts for the meridional and zonal spatial variability of both geopotential and horizontal wind fields, the results based on normal mode energy were tested by two independent analyses.

Normal modes are a useful tool since they allow for the filtering of Rossby waves in both horizontal and vertical spatial scales. The filtering will reduce the noise and makes easier to uncover significant trends in the sensitive vertical structures. However, because 3-D normal modes are global functions, the connection between trends in modal structure and local changes in the physical space is not direct. In order to relate trends in modal structure and local changes in the physical space, we computed the trends in the eddy available potential energy, $A_E(\theta, p) = 1/2 \, c_p \, \gamma \, \overline{T'^2}$, where T' is the temperature deviation from the zonal mean $\overline{T}$, γ is the stability parameter and c_p is the specific heat at constant pressure. We performed this analysis on the NCEP/NCAR reanalysis (NCEP-1 hereafter) and on the three following reanalysis data sets: NCEP/DOE-R2 reanalysis data from NCEP and the Department Of Energy (NCEP-2 hereafter); ERA-40 reanalysis from the European Centre for Medium-Range Weather Forecasts (ECMWF); and the Japanese 25-year Reanalysis (JRA-25) from the Japan Meteorological Agency. The ERA-40 reanalysis covers the period 1958–2001, while the NCEP-2 and the JRA-25 reanalyses cover the period 1980–2008.

The energy A_E was computed for each six-hourly reanalysis time, then it was averaged for the November–April season and finally the interannual trends were obtained for each level and latitude. Besides to show the local changes in the physical space, these calculations also constitute one test to the results obtained with the normal mode energetics.

2.2 Multiple tropopause events

Another test to the hypothesis of an increase of baroclinicity in the UTLS region is given by the analysis of the trends in the frequency of double tropopause events in a subset of radiosoundings. The radiosonde data were obtained from the Integrated Global Radiosonde Archive (Durre et al., 2006) at the NOAA National Climatic Data Center (NCDC). Single and double tropopause events were identified using the World Meteorological Organization thermal lapse rate definition of tropopause (WMO, 1957):

(a) The first tropopause is defined as the lowest level at which the lapse rate decreases to 2 K km^{-1} or less, provided also the average lapse rate between this level and all higher levels within 2 km does not exceed 2 K km^{-1}.
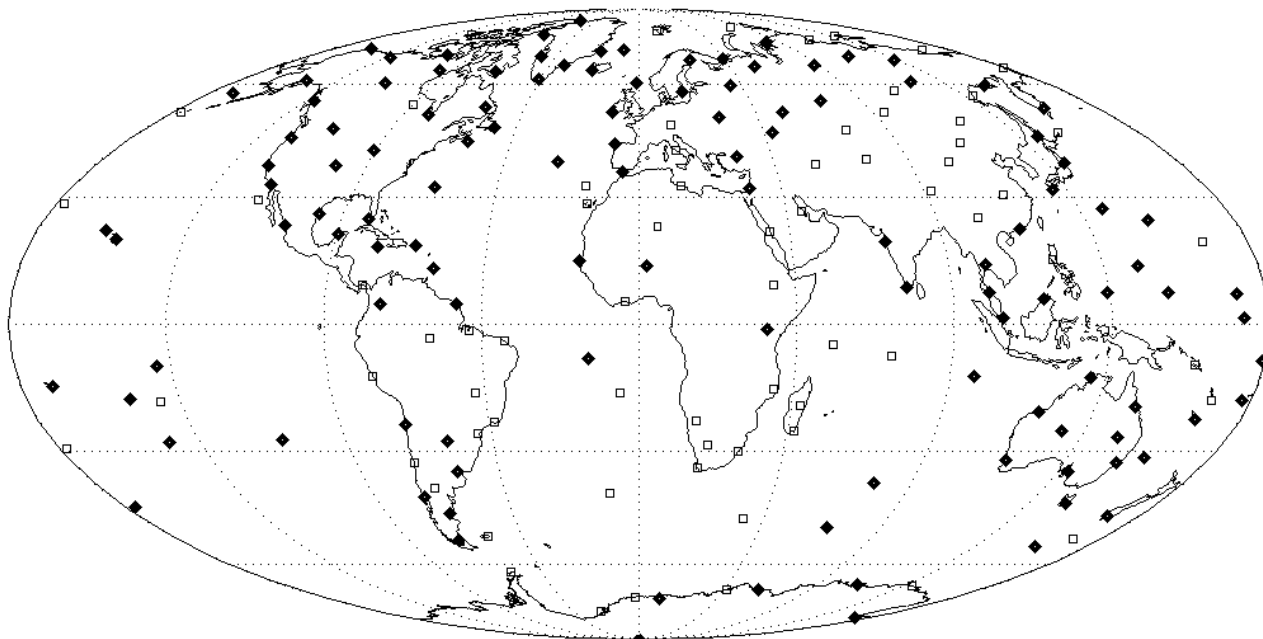
Fig. 2. Radiosonde stations considered in the study of Añel et al. (2008). The solid diamonds represent the stations which passed the homogenization criteria in this work, and which were retained for the computations of the trends in the frequency of double tropopause events.

(b) If above the first tropopause the average lapse rate between any level and all higher levels within 1 km exceeds $3\,\mathrm{K\,km}^{-1}$ then a second tropopause is defined by the same criterion as under (a). This tropopause may be either within or above the 1 km layer.

Daily or twice daily radiosonde observations from a 187-station global network, described by Añel et al. (2008), were analyzed for the 1970–2006 period. The soundings retained in the analysis satisfy the following homogenization criteria: (I) the 50 hPa (70 hPa) level must be reached in the tropics (extratropics); (II) there must be at least one reported level in the vicinity of each of the following mandatory pressure levels: 500, 400, 300, 200, 150, 100, 70, and 50 hPa; (III) the sounding station must report soundings satisfying condition (I) and (II) at least in five different years for each of the following periods: 1970–1979, 1980–1989, 1990–1999, and 2000–2006. Different homogenization criteria were tested. In particular, the trends were recalculated without applying condition (III) or requiring its validity for only two or three decades. Using different conditions (III) imply the inclusion or exclusion of some sounding stations. The results remained qualitatively the same even if all available soundings were considered without the application of any homogenization criterion.

Figure 2 shows the radiosonde stations considered in the study of Añel et al. (2008). The solid symbols represent the stations retained for the computations of the trends in the frequency of double tropopause events.

3 Results

3.1 Baroclinic wave energy trends

The vertical spectrum of the November–April mean energy associated with the baroclinic Rossby waves with wave number $1 \leq s \leq 10$ is shown on the top panel of Fig. 3. The energy peaks at $m=5$ and then decreases monotonically. This energy peaking at $m=5$ suggests again a distinction between the deeper ($m<5$) and the shallower ($m>5$) baroclinic modes. The trends of the energies associated with each of the first nine baroclinic modes are shown on the bottom panel of Fig. 3. The linear change of the energy in the 1958–2006 period is given as a percentage of the mean energy shown in the top panel of Fig. 3. The solid symbols indicate significant trends at the statistical level of 99% ($p=0.01$). The energy values of both high and low frequency waves associated with the deeper baroclinic modes increased during the analyzed period, while the energy associated with the shallower baroclinic modes decreased.

Observing the energy values in the top panel of Fig. 3, it may be concluded that it is the mode $m=4$ which shows the largest absolute trend of energy. Incidently, this vertical mode is the most sensitive to variability in the UTLS region (see Appendix A). Thus, results suggest that most of the increase in baroclinic energy comes from the UTLS region.

Figure 4 shows the time series of the November–April mean energy of Rossby waves with wave numbers $s=1,...,10$. The upper row represents the energy sum for the deeper

baroclinic modes ($m<5$). The left panel shows the time series of the energy of all frequencies and the right panel shows the energy of high frequency waves. Both panels show positive energy trends. The linear increases in the energy of all waves and in the energy of high frequency waves are 10.8% and 13.8% of their respective mean values in the period 1958–2006. The lower row in the figure shows similar time series but for the sum of the energy of the shallower baroclinic modes ($m>5$). In this case, the total and high frequency wave energies present linear decreases of 11.7% and 6.9% of their respective mean values. All linear trends in Fig. 4 are statistically significant at the 99% level.

Particularly remarkable is the fact that the time series of the energy of deeper modes ($m<5$), which are sensitive to the UTLS and the middle stratosphere, do not show significant changes between the trends before and after the year 1979, i.e. between pre-satellite and pos-satellite reanalysis data.

A meridional mode decomposition, similar to the vertical mode decomposition, could, in principle, give information on the horizontal location of the sources of increased baroclinicity. Instead of doing that analysis, we computed the trends in the eddy available potential energy, A_E, of four (NCEP-1, ERA-40, NCEP-2 and JRA-25) reanalysis data sets (Figs. 5 and 6). In order to make more clear the contribution of each latitude band for the total energy measured by the normal modes, Figs. 5 and 6 show the trends in the area weighted eddy available potential energy ($A_E \cos\theta$). The main features of the NH trends are consistently reproduced in the four data sets: the UTLS region is clearly characterized by positive trends in A_E, with a maximum extending from subtropics to midlatitudes; the subtropical and midlatitude lower troposphere is dominated by negative trends. Both in the UTLS and in the lower troposphere there are regions were the trends have high statistical significance, above the 99% level. The trend patterns remain consistent considering both the pre- and pos-satellite period (NCEP-1, ERA-40) and the pos-satellite period only (NCEP-2 and JRA-25). The overall picture in the NH confirms the results of Fig. 3: the energy increase of deeper $m<5$ baroclinic waves must be due to increased baroclinicity in the subtropical and midlatitude UTLS, whereas the energy decrease of shallower $m>5$ baroclinic waves must be due to a decrease of baroclinicity in lower troposphere.

In the Southern Hemisphere (SH), the UTLS positive trends appear shifted poleward, according to the fact that the analysis was performed for the respective warm season, and negative trends are also found in the lower troposphere. However, there are important differences between the NCEP-1 trend pattern and the patterns for ERA-40, NCEP-2 and JRA-25. Whereas the SH troposphere in NCEP-1 reanalysis is dominated by negative trends extending to the UTLS, the ERA-40, NCEP-2 and JRA-25 data sets are dominated by positive trends in the UTLS and a positive center in mid troposphere which extends to the surface at midlatitudes. Comparing the trend patterns of the NCEP-1 reanalysis computed
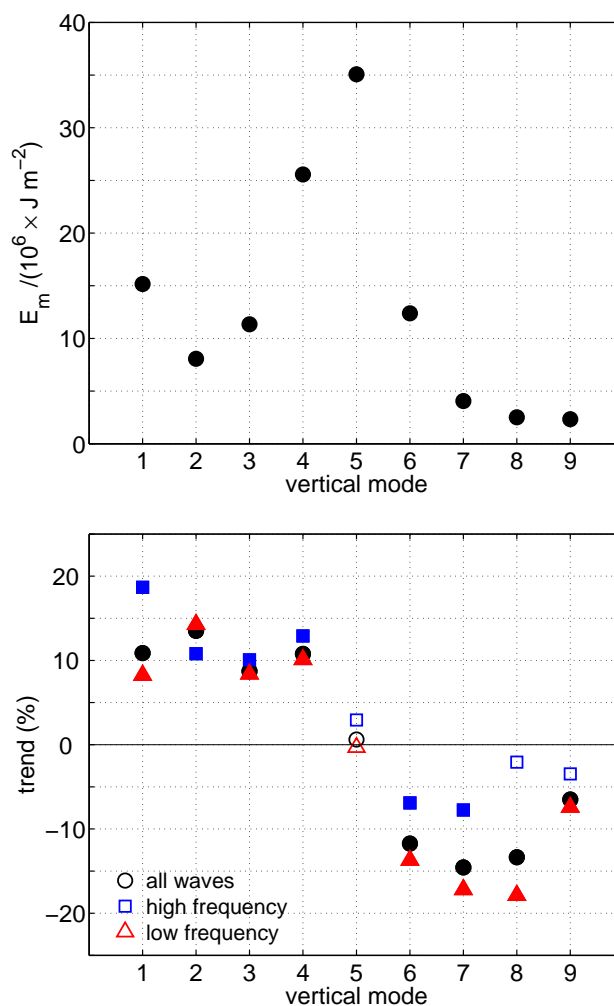

Fig. 3. Top: Vertical spectrum of the mean energy (E_m) associated with the baroclinic Rossby waves of wave numbers $s=1,...,10$. Bottom: Linear trends of the November–April mean energy associated with the Rossby waves of wave numbers $s=1,...,10$, for the first 9 baroclinic modes. The trends are given as percentages of the respective mean energies in the period of 1958–2006. Solid symbols indicate significant trends at the statistical level of 99% ($p=0.01$).

for the pre- and pos-satellite periods (Fig. 7), we may conclude that the main differences between the SH trends of ERA-40, NCEP-2 and JRA-25 and the trends of the NCEP-1 reanalysis are due to the series of the pre-satellite period. A signature of a discontinuity in 1979, probably related to the inhomogeneity in assimilated data with the start of the satellite era, was already apparent in the time series of the energy of shallower modes shown in the lower panels of Fig. 4. It seems that the introduction of satellite data damped the smaller vertical scale circulation components of the NCEP/NCAR assimilation model, producing a discontinuity in the energy of the shallower modes.
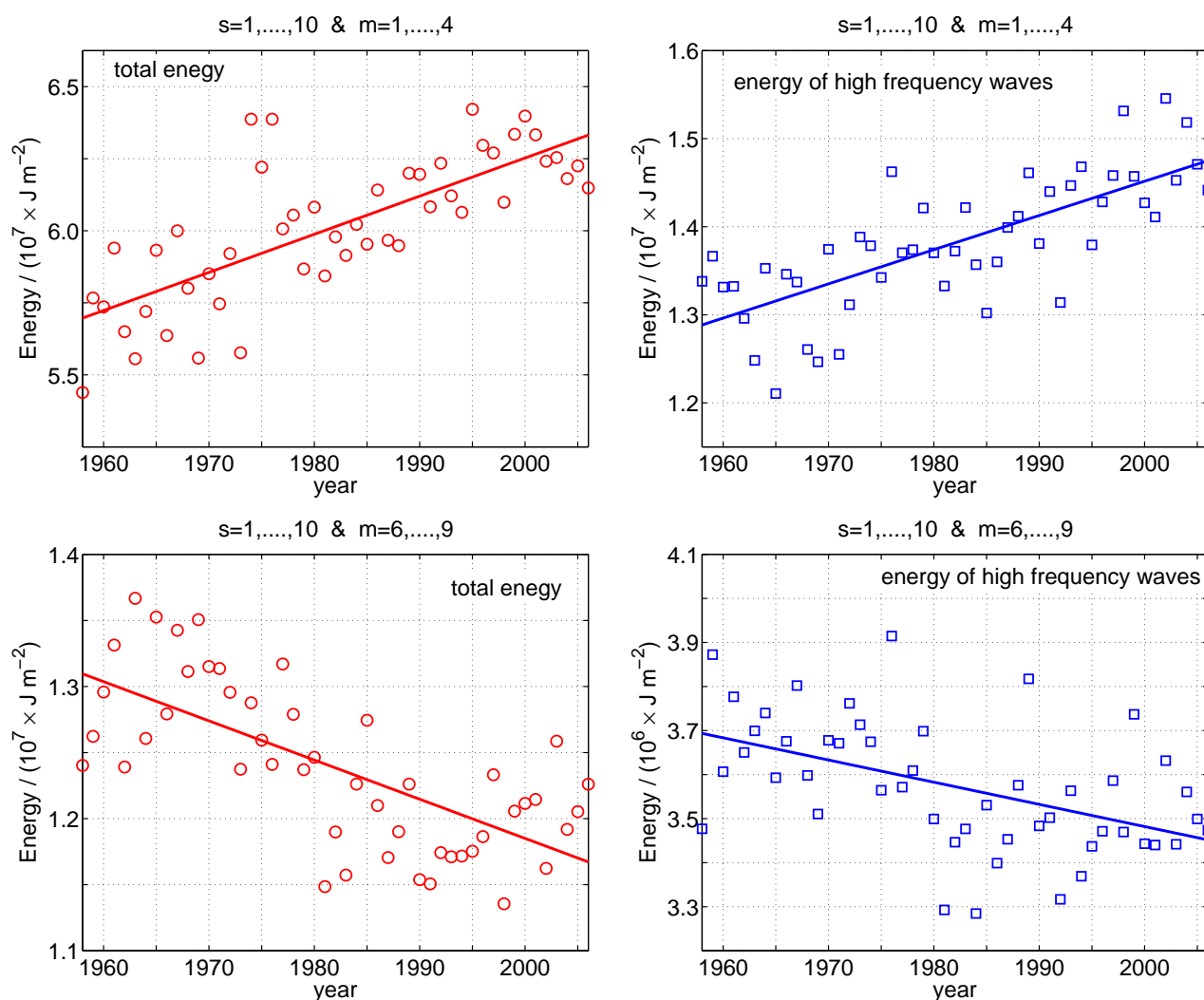
Fig. 4. November–April mean energy associated with baroclinic Rossby waves of wave numbers $s=1,...,10$: (upper row) sum of the energy of the deeper baroclinic modes ($m=1,...,4$), and (lower row) sum of the energy of the shallower baroclinic modes $m=6,...,9$.

3.2 Double tropopause trends

Randel et al. (2007) and, more recently, Pan et al. (2009) showed that the occurrence of double tropopauses is, at least frequently, associated with the tropospheric intrusions of subtropical air into the extratropical lower stratosphere. A secondary tropopause results from a poleward excursion of the tropical tropopause accompanying the movement of the upper tropospheric tropical air over the extratropical tropopause. Pan et al. (2009) also suggested that the occurrence of isolated high latitude events of double tropopauses may result from Rossby wave breaking of subtropical wave ridges. Therefore, at least frequently, the occurrence of double tropopause events is associated with the relative motion of different air mass layers and this relative motion is the typical feature of a baroclinic flow. An event of double tropopause must be associated either with the generation of high frequency baroclinic waves or with the amplification of stationary baroclinic waves, with vertical structures which may explain the circulation variability in the UTLS region. If, as shown in the previous section, the wave baroclinicity of the UTLS has increased during the last five decades, it may also be expected that an increase in the frequency of double tropopause events has occurred. To verify this possibility, we calculated the trends in frequency of double tropopause events in the subset of radiosoundings described in the Data and Method section.

In fact, a general increase in the relative frequency of double tropopause events is found. Figure 8 shows the relative frequency of double tropopause events in the 30°–60° N and 30°–60° S latitudinal belts. These latitudes correspond to the regions where maximum frequency of double tropopause events has been diagnosed in previous studies (Randel et al., 2007; Añel et al., 2008). In the 30°–60° N band there was an
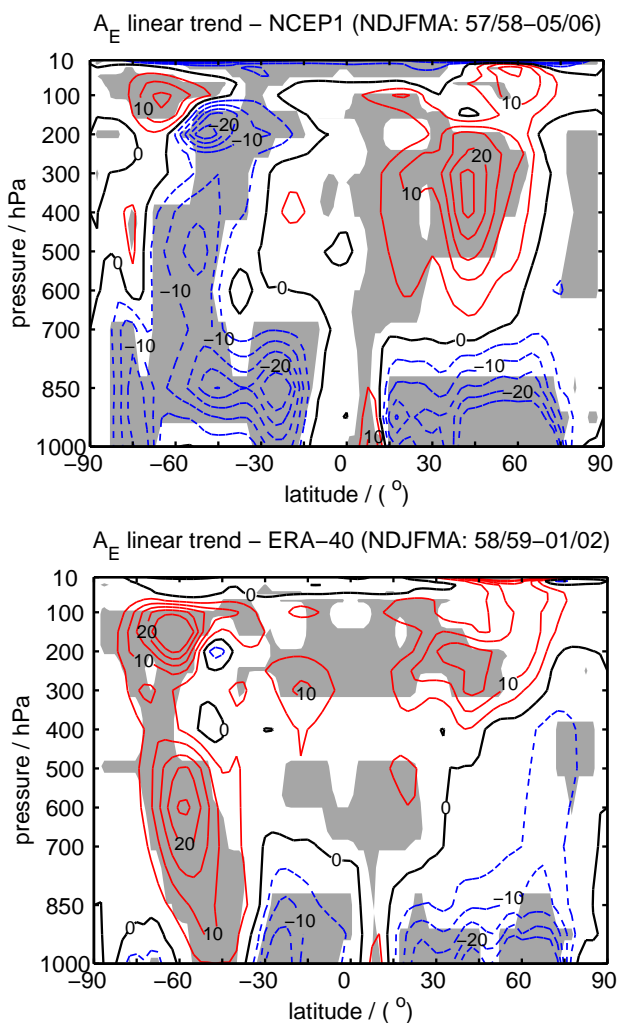
Fig. 5. Interannual trends in the area weighted eddy potential energy ($A_E \cos\theta$) of the NCEP/NCAR (NCEP-1) (top) and ERA-40 (bottom) reanalysis. Units are $\mathrm{J\,m^{-2}\,hPa^{-1}}$ (decade)$^{-1}$. Dashed contours represent negative values, and the shaded areas represent trends statistically significant at the level of 99%.

Fig. 6. As in Fig. 5 but for the NCEP-2 (top) and JRA-25 (bottom) reanalysis.

increase of 4.8% (3.3%) per decade in the cool season (annual mean) frequency of double tropopause events. For the same calendar periods, the frequency of double tropopause events in the band 30°–60° S increased 5.7% (6.6%) per decade in the warm season (annual mean). All these trends are statistically significant at the 99% level. As it may be concluded by the comparison of the seasonal (November–April) and annual frequencies, the double tropopause events are more frequent during the cool season in each hemisphere. Such results also match with the above suggested importance of baroclinicity for the occurrence of double tropopause events.

The trends in the relative frequency of double tropopause are stronger in the Southern Hemisphere. This is consistent with the larger cooling trends observed in the Antarctic
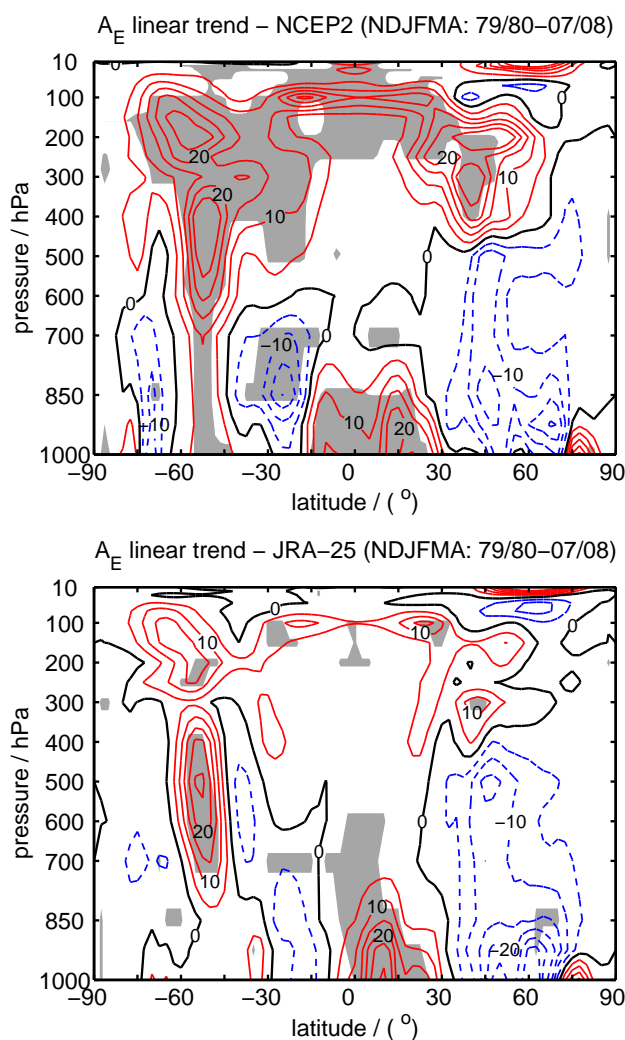
lower stratosphere during spring and summer (September to February), in association with the development of the Antarctic ozone hole (Randel et al., 2009; Schwarzkopf and Ramaswamy, 2008). In fact larger cooling trends at high southern latitudes should imply a larger trend in the equatorward temperature gradient and a corresponding increase of UTLS baroclinicity.

4   Concluding remarks

Observational evidence of an increase of midlatitude UTLS wave baroclinicity during the last five decades is presented in this study. As mentioned in the introductory section, the simulated response of climate models to the increase of greenhouse gas radiative forcing is quite consistent, showing a deep warming of the tropical troposphere and cooling of the stratosphere. This warming and cooling pattern leads to the
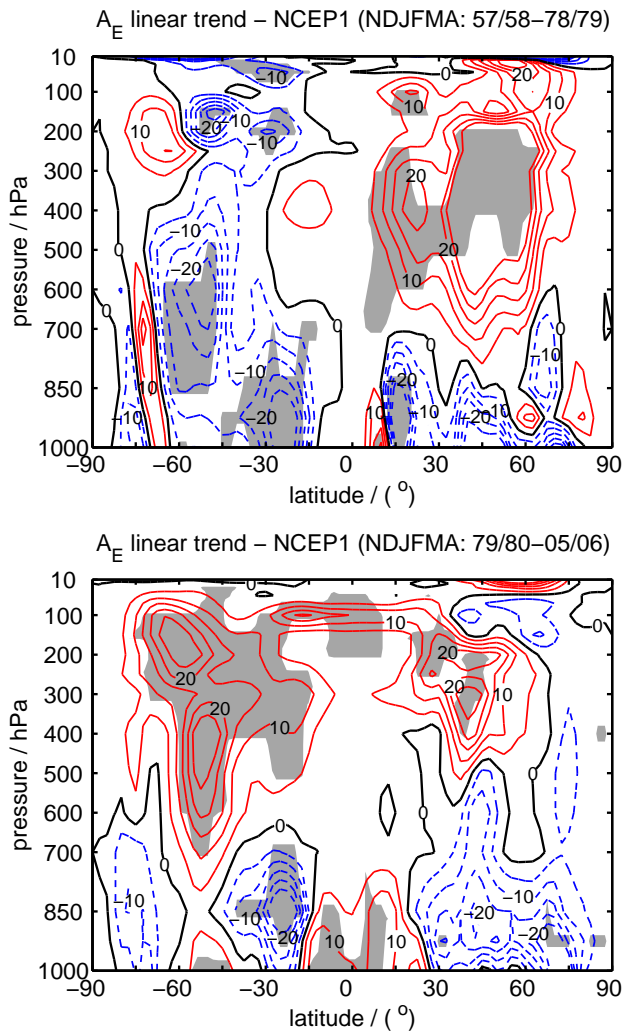
Fig. 7. As in Fig. 5 but for the NCEP/NCAR (NCEP-1) reanalysis in pre-satellite (top) and in the pos-satellite data periods.

strengthening of meridional thermal gradients in the subtropical and midlatitude UTLS regions. Since positive trends in the UTLS equatorward thermal gradients, during the last three or four decades, have been confirmed by several recently published observational studies, our results may constitute another evidence of climate change due to changes in radiative forcing agents.

The results here presented are very robust because they remained basically the same considering different methods of analysis and different data sets.
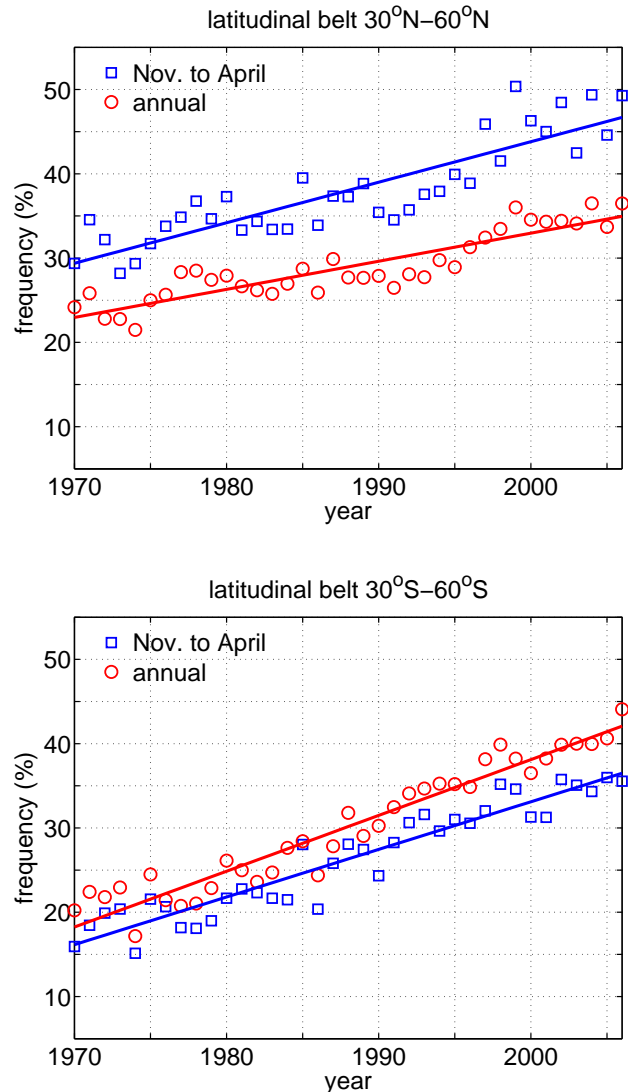

Fig. 8. Relative frequency of double tropopause events in the 30° N–60° N (upper panel) and 30° S–60° S (lower panel) latitude belts.

Appendix A

3-D normal mode scheme

The normal mode complex amplitudes, $w^{\alpha}_{\mathrm{msl}}$, are obtained by means of a vertical projection onto the vertical structure functions

$$(\hat{u}, \hat{v}, \hat{\phi})^T_m = \frac{1}{p_s} \int_0^{p_s} (u, v, \phi)^T G_m(p) dp, \qquad (A1)$$

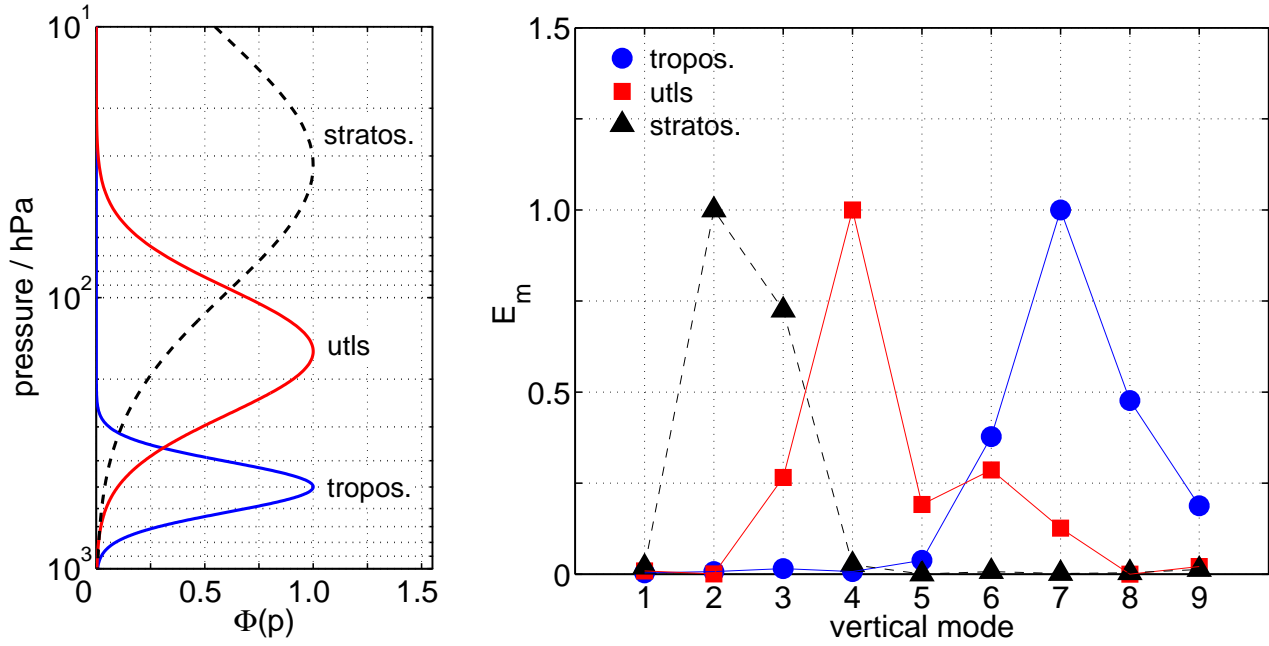followed by an horizontal projection onto the horizontal structure functions

Fig. A1. Vertical energy spectra (right) of three idealized geopotential anomalies (left) centered at the middle troposphere, in the UTLS region and in the middle stratosphere. The spectra and the anomalies were normalized to their respective maxima.

$$w_{\mathrm{msl}}^{\alpha} = \frac{1}{2\pi} \int_0^{2\pi} \int_{-\pi/2}^{\pi/2} \left(\mathbf{H}_{\mathrm{msl}}^{\alpha}\right)^* \mathbf{C}_m^{-1} \tag{A2}$$

$$\cdot (\hat{u}, \hat{v}, \hat{\phi})_m^T \cos\theta \, d\theta \, d\lambda,$$

where it is assumed that the vertical structure functions, $G_m(p)$, and the horizontal structure functions, $\mathbf{H}_{\mathrm{msl}}^{\alpha}(\lambda, \theta) = \exp(is\lambda) \left[U(\theta), iV(\theta), Z(\theta)\right]_{\mathrm{msl},\alpha}^T$, have unitary norms. Superscripts T and $()^*$ respectively denote the transpose and the complex conjugate of the transpose. The constant pressure, p_s, represents a prescribed isobaric surface near the Earth's surface. In our calculations, we chose p_s as the mean sea-level pressure of the NCEP/NCAR reanalysis dataset (p_s=1011.3 hPa).

For $s \geq 1$, the total (i.e. kinetic + available potential) energy per unit area associated with a given mode is proportional to the squared norm of the respective complex amplitude, $w_{\mathrm{msl}}^{\alpha}$ (Liberato et al., 2007, and references therein)

$$E_{msl}^{\alpha}(t) = \frac{p_s h_m}{2} |w_{msl}^{\alpha}(t)|^2. \tag{A3}$$

The projection onto the horizontal modes allows for the decomposition of circulation field into inertio-gravity and Rossby waves. However, if we do not separate these waves and perform only the vertical decomposition, the energy associated with a vertical mode m is given by

$$E_m = \frac{p_s}{4\pi \, g} \int_0^{2\pi} \int_{-\pi/2}^{\pi/2} \left(\frac{\hat{u}_m^2 + \hat{v}_m^2}{2} + \frac{\hat{\phi}_m^2}{2 \, g \, h_m}\right) \tag{A4}$$

$$\cos\theta d\theta \, d\lambda.$$

A1 Energetics of idealized anomalies

Consider an idealized gaussian geopotential anomaly given by

$$\phi(\lambda, \theta, p) = A \sqrt{\frac{p_s}{p}} \exp\left[-\left(\frac{z - z_0}{B}\right)^2\right] \psi(\lambda, \theta) \tag{A5}$$

where A, B and z_0 are constants, ψ represents the horizontal structure of the anomaly field, and $z = -H \ln(p/p_s)$, with H=7 km. Using geostrophy, the energy of vertical mode m will be given by

$$E_m = \frac{p_s}{4\pi \, g} \frac{\hat{\Phi}_m^2}{2} \int_0^{2\pi} \int_{-\pi/2}^{\pi/2} \tag{A6}$$

$$\left[\frac{\psi^2}{g \, h_m} + \left(-\frac{1}{f \, a} \frac{\partial \psi}{\partial \theta}\right)^2 + \left(\frac{1}{f \, a \cos\theta} \frac{\partial \psi}{\partial \lambda}\right)^2\right]$$

$$\cos\theta d\theta \, d\lambda$$

where f is the Coriolis parameter and $\hat{\Phi}_m$ is the vertical projection of the pressure dependent part of the anomaly field.
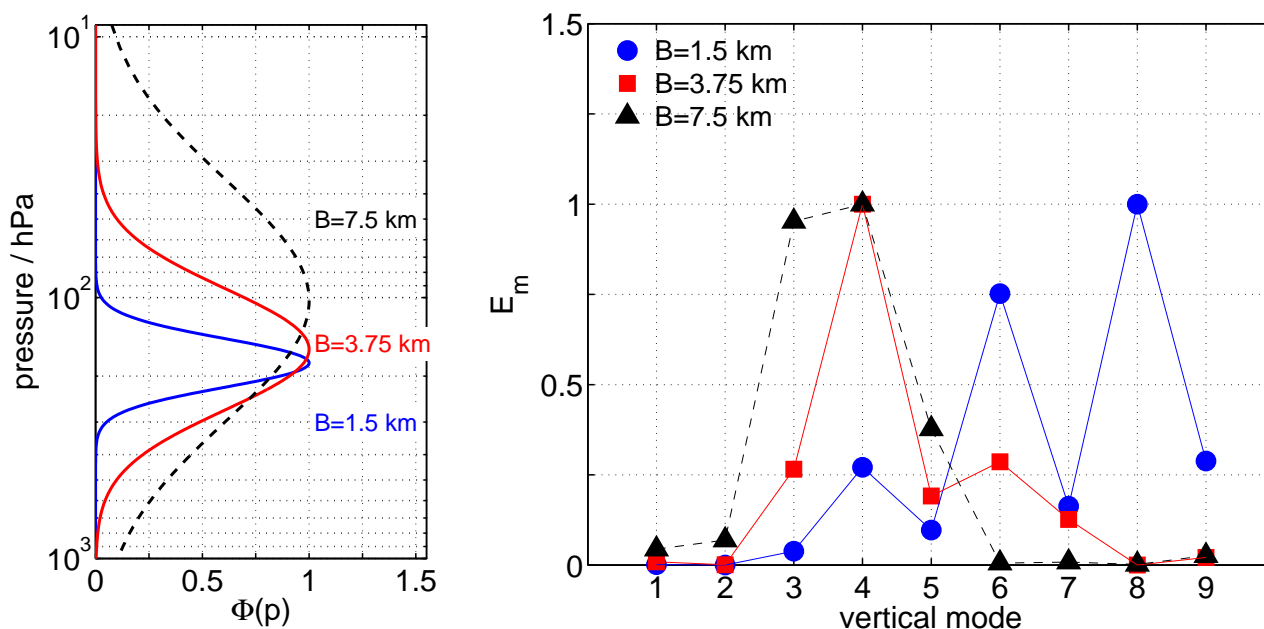
Fig. A2. As in Fig. A1 but with all anomalies centered at the level (z_0=12 km) inside the UTLS.

Considering that the zonal and meridional spatial scales of ψ are L_x and L_y, respectively, the energy is approximated by

$$E_m \cong \frac{p_s}{4\pi\ g}\ \frac{\hat{\Phi}_m^2}{2}\left[\ \frac{1}{g\ h_m} + \left(\frac{1}{f\ L_y}\right)^2 + \left(\frac{1}{f\ L_x}\right)^2\ \right] \qquad (A7)$$

$$\int_0^{2\pi}\int_{-\pi/2}^{\pi/2}\psi^2\cos\theta d\theta\ d\lambda.$$

The left panel in Fig. A1 shows the vertical profile of three idealized anomaly fields. The constants in Eq. A5 were chosen to reproduce anomalies centered at the middle troposphere, in the UTLS region and in the middle stratosphere.

Both the anomaly fields and the respective energy spectra (Fig. A1, right panel) were normalized to their respective maximum values. The energy spectra were calculated considering $(f\ L_x)^2 = (f\ L_y)^2 \sim 10^5$, corresponding to spatial scales between 10^6–10^7 m for a central latitude of 45°. If we choose $L=10^6$ m or $L=10^7$ m , the spectra remain qualitatively the same. As it may be observed, the shallower modes ($m>5$) represent tropospheric anomalies, whereas the deeper modes ($m<5$) represent anomalies in the UTLS and in the stratosphere.

The constant B, in Eq. A5, represents the vertical scale of the anomalies. The circulation anomalies confined to the lower troposphere must have a small vertical scale, whereas the anomalies in the UTLS and in the stratosphere may have larger vertical scales. To simulate the tropospheric, the UTLS, and the stratospheric anomaly profiles of Fig. A1, we used B=1.5, 3.75 and 7.5 km, respectively. In order to assess the effect of the vertical scale of the anomalies on the projections, Fig. A2 shows the energy spectra of three anomalies

with the same vertical scales, B, as in Fig. A1 but all centered at the same level z_0(=12 km) of the UTLS anomaly. As may be observed, small scale anomalies in the UTLS project on the shallower modes, whereas the large vertical scales project on the deeper modes. This result illustrates the vertical scale filtering associated with the projections onto the vertical structure functions.

References

Allen, R. J. and Sherwood, S. C.: Warming maximum in the tropical upper troposphere deduced from thermal winds, Nat. Geosci., 1, L03705, doi:10.1038/ngeo208, 2008.

Añel, J. A., Antuña, J. C., Torre, L. de la, Castanheira, J. M. and Gimeno, L.: Climatological features of global multiple tropopause events, J. Geophys. Res., 113, D00B08, doi:10.1029/2007JD009697, 2008.

Durre, I., Vose, R. S., and Wertz, D. B.: Overview of the Integrated Global Radiosonde Archive, J. Climate, 19, 53–68, 2006.

Eichelberger, S. J. and Hartmann, D. L.: Changes in the strength of the Brewer-Dobson circulation in a simple AGCM, Geophys. Res. Lett., 32, L15807, doi:15810.11029/12005GL022924, 2005.

Eyring, V., Butchart, N., Waugh, D. W., et al.: Assessment of temperature, trace species, and ozone in chemistry-climate model simulations of the recent past, J. Geophys. Res., 111, D22308, doi:10.1029/2006JD007327, 2006.

Garcia, R. R. and Randel, W. J.: Acceleration of the BrewerDobson Circulation due to Increases in Greenhouse Gases, J. Atmos. Sci., 65, 2731–2739, doi:10.1175/2008JAS2712.1, 2008.

Geng, Q. and Sugi, M.: Possible Change of Extratropical Cyclone Activity due to Enhanced Greenhouse Gases and Sulfate AerosolsStudy with a High-Resolution AGCM, J. Climate, 16, 2262–2274, 2003.

Hoskins, B. J., McIntyre, M. E. and Robertson, A. W.: On the use and significance of isentropic potential vorticity maps, Q. J. Roy. Meteorol. Soc., 111, 877-946, 1985.

Juckes, M.: The Structure of Idealized Upper-Tropospheric Shear Lines, J. Atmos. Sci., 56, 2830–2845, 1999.

Kanukhina, A. Yu., Suvorova, E. V., Nechaeva, L. A., Skrygina, E. K., and Pogoreltsev, A. I.: Climatic variability of the mean flow and stationary planetary waves in the NCEP/NCAR reanalysis data, Ann. Geophys., 26, 1233–1241, 2008, http://www.ann-geophys.net/26/1233/2008/.

Liberato, M. L. R., Castanheira, J. M., de la Torre, L., DaCamara, C. C., and Gimeno, L.: Wave Energy Associated with the Variability of the Stratospheric Polar Vortex, J. Atmos. Sci., 64, 2683–2694, 2007.

Pan, L. L., Randel, W. J., Gille, J. C., et al.: Tropospheric intrusions associated with the secondary tropopause, J. Geophys. Res., 114, D10302, doi:10.1029/2008JD011374, 2009.

Ramaswamy, V. and Schwarzkopf, M. D.: Effects of ozone and well-mixed gases on annual mean stratospheric temperature trends, Geophys. Res. Lett., 29(22), 2064, doi:10.1029/2002GL015141, 2002.

Randel, W. J., Seidel, D. J., and Pan, L. L.: Observational characteristics of double tropopauses, J. Geophys. Res., 112, D07309, doi:10.1029/2006JD007904, 2007.

Randel, W. J., Shine, K. P., Austin, J., et al.: An update of observed stratospheric temperature trends, J. Geophys. Res., 114, D02107, doi:10.1029/2008JD010421, 2009.

Schwarzkopf, M. D., and Ramaswamy, V.: Evolution of stratospheric temperature in the 20th century, Geophys. Res. Lett., 35, L03705, doi:10.1029/2007GL032489, 2008.

Thorpe, A. J.: Diagnosis of balanced vortex structure using potential vorticity, J. Atmos. Sci., 42, 397–406, 1985.

World Meteorological Organization: Meteorology - A threedimensional science: Second session of the Commission for Aerology, WMO Bulletin, IV(4), 134-138, 1957.